Electronic Supplementary Information

Impact of water on the lubricating properties of hexadecane at the nanoscale

Clodomiro Cafolla and Kislon Voïtchovsky

Physics Department, Durham University, Durham DH1 3LE, UK

email: kislon.voitchovsky@durham.ac.uk

Index of content

1. Cleaning procedures

Extensive cleaning procedures were implemented to ensure reliably of the results. Hexadecane and oleic acid were stored in borosilicate bottles (Pyrex, Corning, NY, USA). Glass containers were subject to the following protocol before use. First, they were washed with tap water and soap, then rinsed with tap water 20 times, followed by ultra-pure water (18.2 MΩ, Merck Millipore, Billerica, MA, USA), > 98% pure propan-2-ol (Merck Millipore, Billerica, MA, USA), and finally ultra-pure water. The propan-2-ol was used without any further purification. The glass containers were then extensively flushed with nitrogen in order to remove remaining water.

AFM cantilevers were immersed in a bath of ultrapure water, followed by propan-2-ol, and finally ultrapure water again. Each step lasted for at least 60 minutes. A nitrogen flux was used to dry the cantilevers.

The AFM stage was cleaned firstly ultra-pure water, then pure propan-2-ol (Merck Millipore, Billerica, MA, USA), and finally with ultra-pure water again. The stage was heated to 120 °C for 30 minutes before each experiment to evaporate residual water and possible contaminants from previous experiments.

2. Representative results: from raw measurement outputs to viscoelastic data

Shear force spectroscopy as operated here effectively uses the AFM as a nanoscopic linear rheometer, with the liquid confined between the tip apex and the surface being probed. This allows for highly localised measurements of the lubricant's viscoelastic properties while quantifying the resulting lubricated friction down to the pN range. The method has been pioneered in the labs of E. Riedo[1,2], and further developed by our group[3–5].

Practically, the shear measurements are conducted as follows. Lateral oscillations are imposed to the sample using the AFM scanner. To ensure locality of the measurement, the imposed oscillation amplitude is kept below 1 nm (here 0.5 nm). The frequency is set at 1.1 kHz, below the resonance frequency of the scanner (~2 kHz) so as to avoid hardware damage. Both, the amplitude and the frequency can be changed externally; the parameters used here represent a

compromise between accuracy and rapidity. As the tip approaches the sample's surface, the cantilever experiences some lateral torsion due to coupling through the confined liquid. This occurs typically in the last nanometer before contact, and increases progressively as the tip presses on the surface. Detection of the amplitude and phase of torsion are achieved using the AFM lock-in amplifier set on the lateral oscillation frequency. Given the geometry of the system, the torsional amplitude and phase represent the shear amplitude and phase respectively. Simultaneously, the normal force exerted by the tip on the confined liquid is obtained from the average vertical cantilever deflection. A typical shear-extension curve is shown in Fig. S1. Positive values of the base extension (Z-piezo) indicate the true tip-sample distance, whereas negative values describe the region where the tip does not move vertically but the applied vertical load increases. When the tip-surface is larger than a few nanometers, no liquid confinement occurs and no coupling exists between the tip and the moving solid surface. The shear amplitude is close to zero and the phase exhibits random oscillations between 0° and 90°. As the tip moves to the surface, viscoelastic coupling start to occurs though the liquid. The shear amplitude increases (here linearly) with the confining force; and the shear phase evolves from an almost perfectly viscous coupling (90°) to a viscoelastic regime as more load is applied, consistently with the reduction in configurational entropy of the confined liquid[4,5]. In this repulsive regime, and for small z-displacements, the cantilever follows a Hookean behaviour thus allowing extracting the force applied, F_L, by the tip during the shearing:

$$F_L = k_f \, d \qquad (s1)$$

where k_f and d are the flexural spring constant and vertical deflection, respectively[4–6]. The same reasoning can be used for the small induced torsional amplitudes, A_t, which is related to the shear force, F_S, through:

$$F_S = k_t \, A_t \qquad (s2)$$

where k_t is the torsional spring [4–6].

When focusing on the repulsive region, it is convenient to plot the shear amplitude and phase as functions of the vertical deflection (or applied load). This is done in Figs 4 and 5 of the paper. This approach offers two main advantages. First it allows for an estimate of the confining pressure between the tip and the mica surface. The confinement area being about 100 nm^2 (see below ESI Section 6), the confining pressure increases by ~10 MPa for every nN applied.

Second, the non-contact region when no coupling takes place, is reduced to a single point, thus focusing on the most meaningful part of our data set.

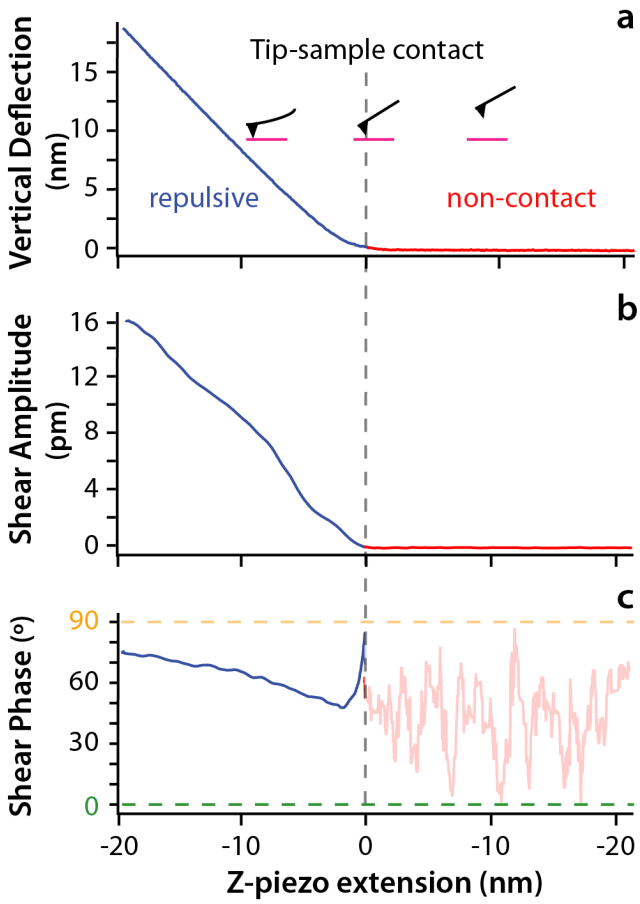

Fig. S1. Example of a single shear-force spectroscopy measurement. *The vertical cantilever deflection (top), the torsional amplitude (middle) and the associate torsional phase (bottom) as measured simultaneously as functions of the vertical extension of the cantilever base (AFM Z-piezo). The shear amplitude is always taken as peak to peak. The cartoons in the top subplot illustrate the position of the tip with respect to the sample surface at different Z-piezo extensions. The dotted vertical line marks the beginning of a permanent vertical deflection (repulsive) and the Z-piezo extension is arbitrarily set to zero, marking the measured point of contact between the tip and the sample. The induced torsional (or shear) amplitude being too small before the point of contact, the phase is undefined (semi-transparent region in the bottom subplot) and randomly oscillates between the extreme values of perfectly elastic (0°) and viscous couplings (90°). The experiment was performed on hexadecane adsorbed on mica and using an arrow cantilever. The RH and temperature were 46 ± 2% and 25.0 ± 0.1 °C, respectively.*

In a typical experiment, measurements were taken over at least 5 locations, with at least 20 individual set of force curves (as shown in Fig. S1) per location. A Python code was used to sort out automatically all the acquired data curves into relevant folders. The curves were then suitably plotted, adjusted (force calculation) and averaged using a bespoke routine in Igor Pro

(Wavemetrics, Lake Oswego, OR, USA). Only the extension curves (tip approaching the surface) are considered for the analysis in order to be systematically probing the interface from its equilibrium arrangement and allow for better comparability and reproducibility. Retraction curves were also acquired and usually exhibit an identical behaviour to the extension curves (not shown) aside for occasional variations likely induced by tip-induced transient changes in the interfacial molecular arrangement.

The present shear force measurements contrast with standard friction force microscopy. First, the measurements are highly localised (within a few square nanometers) allowing distinction between contributions from the hexadecane interface and water nanodroplet. The technique could be used elsewhere to probe the lubrication properties of single ions[4] and surface nano-defects[5]. Second, using a spectroscopic approach allows for probing a whole range of applied loads in a same measurement at any given location. This additional information helps interpret the organisation and dynamics of the fluid and distinguish between e.g. repulsive van der Waals, solvation hydration forces and double layer forces[7].

3. Control of the shear phase as an accurate parameter for quantifying viscoelasticity

In standard rheology measurements conducted with a linear rheometer, the shear phase characterises the viscoelastic properties of the fluid under shear. Here, the torsional phase is interpreted as shear phase in the same framework. In order to ensure that this interpretation can be used in the present context, we need to test it on a system where the phase can be predicted. This control is necessary because of the technical limitations in the AFM set-up that could, in principle, introduce an additional phase lag between the reference oscillation applied to the scanner and the measured tip torsion.

Here, we use a mica surface immersed in pure water as our control sample. Shear curves are acquired continuously while progressively increasing the Z-piezo extension and hence the applied load. The experiment is presented in Fig. S2, with all the curves appearing in different colours on the same graphs.

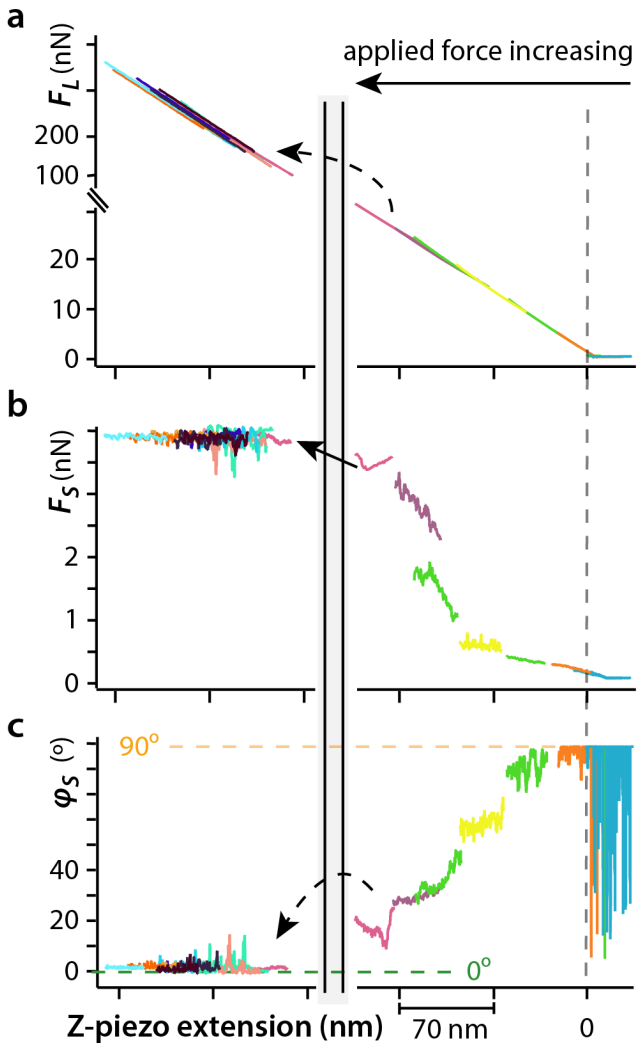

Fig. S2. Shear measurement with increasing confining forces in pure water. *The applied force, F_L, shear force, F_S, and the shear phase, φ_S, were acquired simultaneously for each spectroscopic curves (all different colours). Multiple curves are acquired as the Z-piezo is progressively extended to increase the applied load. In proximity of the point of contact (vertical dotted line), $F_S > 0$ and $\varphi_S \sim 90°$. As F_L increases, the shear force eventually reaches a plateau due to the tip pinned into the mica (left region of the graphs). The transition to the plateau coincides with the shear phase converging to zero within error. This confirms the validity of the data interpretation and the reliability of the shear phase to characterise the viscoelasticity of the system. The RH and temperature were 46 ± 2% and 25.0 ± 0.1 °C, respectively.*

Before the tip experiences any coupling with the oscillating surface (Z-piezo > 0), the shear force was close to zero and the shear phase is undefined. This is consistent with the behaviour visible in Fig. S1. When the tip reaches the surface (Z-piezo extension close to zero), the tip starts experiencing some coupling (dotted vertical line); the shear force increases and the shear phase is ~90° within error. This is in agreement with the hypothesised perfectly viscous behaviour of water for such a soft nano-confinement. As the Z-piezo extends (negative values),

the applied load increases and the shear phase decreases, indicating an increase of the confined liquid's elastic component.

At loads > 100 nN, the tip is pinned into the mica surface. The shear force reaches a maximum and the shear phase goes to zero. This is expected for a perfectly elastic behaviour[1,4], here artificially created by pinning the tip into the sample. Given the high loads (~350 nN) applied to the tip, significant damage was done to both the tip and the sample. This type of measurement was hence conducted only once as a control.

4. Impact of humidity on interfacial water nanodroplets

In order to unambiguously establish the role of water in our model system, control experiments were carried out at different relative humidity (*RH*). The mica disc and the AFM chamber were flushed with pure nitrogen for 48 hours so as to reach $RH = 0\%$ within experimental error (± 2%). The AFM experiments were then conducted without the nitrogen flow to avoid acoustic perturbations, resulting in $RH < 10\%$ throughout the measurements (low humidity). In this case, no nanodroplets appeared at the interface, even after increasing the temperature up to 95 °C (Fig. S3). In contrast, when equilibrating the mica substrate at $RH > 75\%$ for 2 hours and then running the experiments at the same humidity level, nanodroplets were already present at room temperature. Such a high *RH* was achieved by saturating the AFM chamber with water vapour.

The nucleation of water nanodroplets at the interface has a dramatic influence on the lubricated friction. At low *RH*, shear forces reveal a standard thermal behaviour[3,5] with the lubricated friction force decreasing with temperature. This is no longer true at higher *RH* where temperature increases the lubricated friction force due to the presence of nanodroplets at the interface.

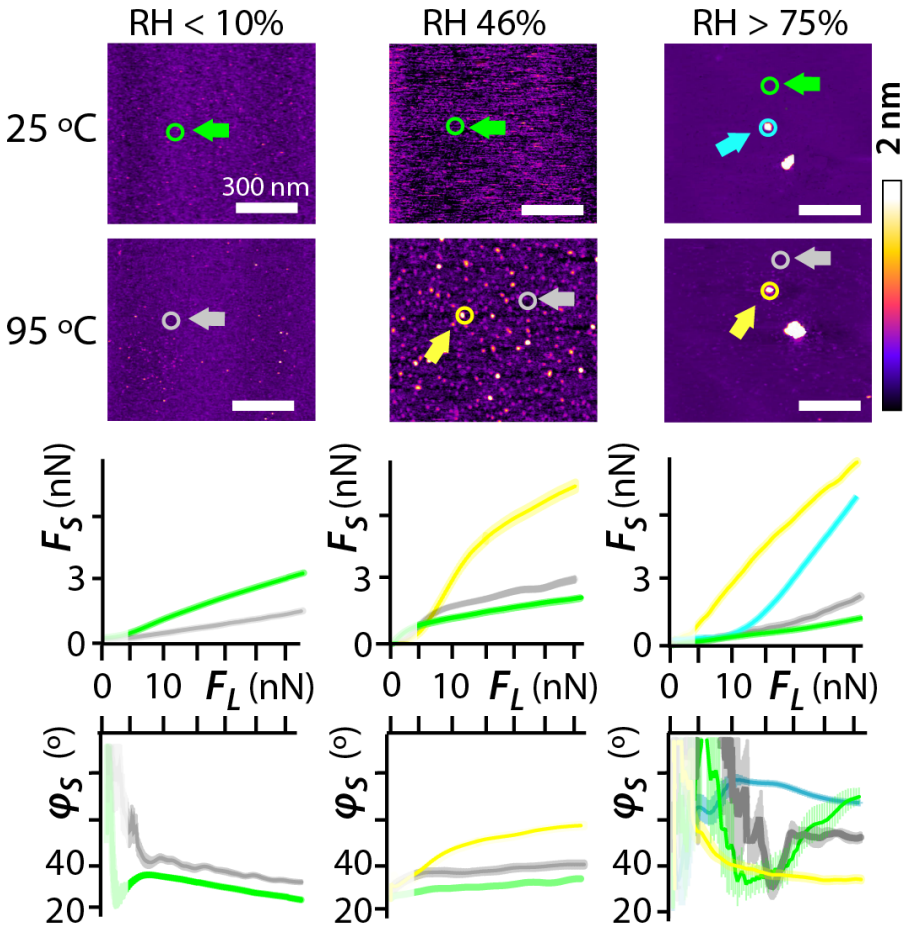

Fig. S3. Nanoscale impact of relative humidity on lubrication. *High-resolution amplitude-modulation AFM imaging of hexadecane at the mica interface with mica (top). At low RH, no water nanodroplets appear at the interface and the lubricated friction force (shear force F_s) decreases with increasing temperature. As the RH increases, water nanodroplets begin to appear with a significant impact on F_s. For RH of 46% (ambient conditions) and 75%, F_s is dramatically influenced by the presence of nanodroplets. This results in an anomalous thermal behaviour of F_s with temperature. For low and intermediate RH, the shear phase φ_S values indicate a viscoelastic regime with a weak evolution towards a more viscous behaviour as the temperature increases. At intermediate RH, the presence of nanodroplets create a more viscous shearing, consistent with the behaviour of water under shear*[4]*. At higher RH, nanodroplets tend to dominate the shear response of the lubricant. At low confining forces (< 5 nN), the shear amplitude is close to the experimental noise level, and the associated phase is undefined (semi-transparent regions). For all the RHs probed, the green and cyan force curves are taken respectively on areas of uniform hexadecane-mica interface and nano-droplets at 25 °C; the grey and yellow curves are taken respectively on areas of uniform hexadecane-mica interface and nano-droplets at 95 °C. The error on the RH is ± 2%.*

5. Control experiments to rule out contamination effects

5.1 Controls for the substrate and the liquids

In order to rule out the possibility of the AFM observations of nanodroplets being the result of contamination, each experiment was performed 5 times using different batches of hexadecane and mica discs and consistently showing interfacial nanodroplets. Control experiments were also carried out using a silicon nitride AFM probe and a hydrophobic substrate, highly orientated pyrolytic graphite (HOPG). The hydrophobic nature of HOPG prevents the formation of a stable water layer in ambient conditions[4] while favouring the adsorption of organic contaminants and should therefore not allow for water nanodroplets to form.

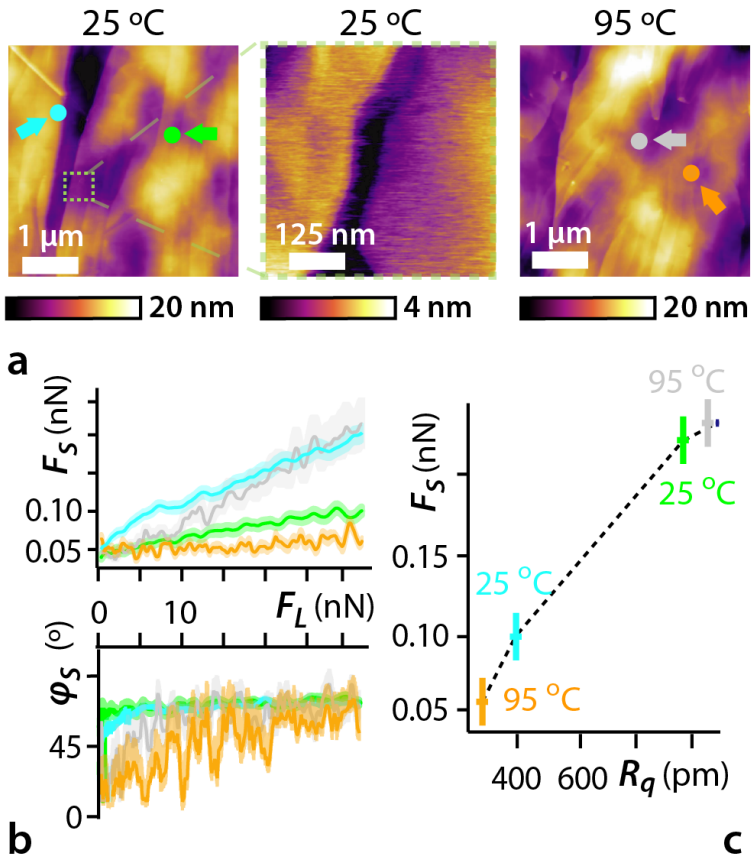

Fig. S4. AFM imaging and shear behaviour of hexadecane molecules at the surface of HOPG. *Topography images (top) clearly show step edges and molecular layers, but no nanodroplets similar to those in Figs 1, 4 and 5. Experiments were performed at RH = 45 ± 2%.* ***(a)*** *Shear force spectroscopy measurements reveal a standard decrease of the lubricated friction force (shear force F_S) with temperature.* ***(b)*** *The confined hexadecane layer shows a consistent viscoelastic behaviour as confirmed by the shear phase φ_S.* ***(c)*** *The friction force is primarily affected by surface singularities such as steps and roughness, as shown by the clear correlation between the lubrication force and the root mean square roughness (R_q) of the HOPG.*

Representative images (Fig. S4) confirm the absence of nanodroplets regardless of temperature. In the absence of water, the shear response of the lubricant is dominated by surface nano-defects as already known from other model systems[5]. Interestingly, even close to the surface singularities, the lubricated friction force is significantly smaller than that induced by water nanodroplets (see Figs 4 and 5). This highlights the dominating role of interfacial water.

5.2 Controls for the AFM tip

To rule out the possibility of the nanodroplets being a tip-induced effect and ensure the validity of our observations, we repeated a set of experiments with a hydrophobic diamond probe and the same hexadecane-mica system. The results, shown in Fig. S5, confirm the presence of water nanodroplets, here already visible at low temperature due to the stochastic nature of the nucleation process. The interfacial density of the droplets increases with temperature as can be expected. This control experiment fully supports the nucleation of water-nanodroplets as the main cause for the observed features.

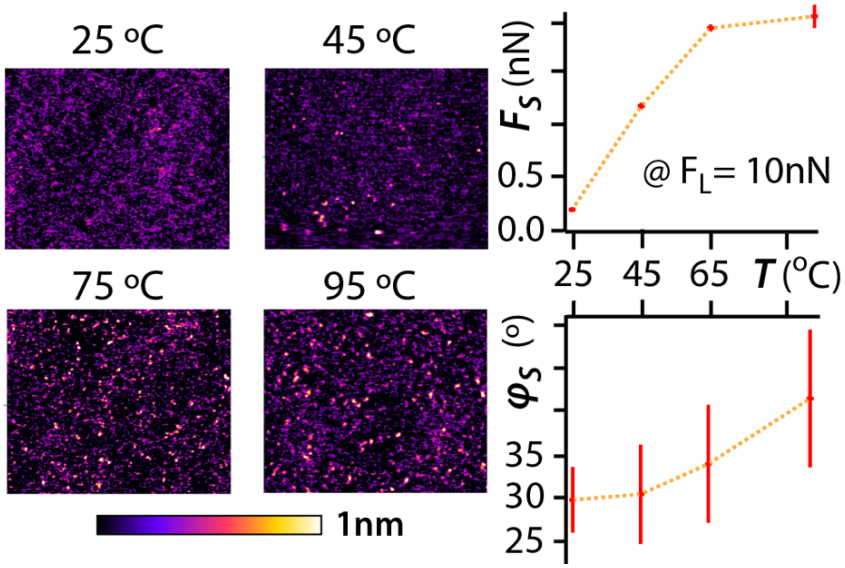

Fig. S5. High resolution imaging and shear behaviour of the hexadecane-mica interface measured with a diamond AFM tip. *Topographic images of the interface show the density of nanodroplets to increase with temperature. At each temperature, the shear force F_S and phase φ_S are averaged over at least 5 locations to show the average impact of the nanodroplets, revealing the unusual increase of F_S with temperature. The associated shear phase shows a viscoelastic response of the sheared lubricant with no obvious temperature effect. The shear forces and phases displayed correspond to an applied load of F_L = 10 nN. Experiments were performed at RH = 45 ± 2%.*

6. Scanning Electron Microscopy analysis of the AFM probes

Four randomly selected cantilevers were analysed by scanning electron microscopy (SEM) before and after imaging and conducting shear-force measurements. Before SEM imaging, the AFM probes were sputtered with a 15 nm thick gold-coating in order to reduce any charge accumulation. The SEM analysis was carried out with a commercial FEI Helios SEM system (Dawson Creek Drive Hillsboro, Oregon 97124 USA). The machine operated at 3 kV electron beam in vacuum with a current set to 0.17 nA. Representative images shown in Fig. S6 do not show any significant changes before and after the experiments. The absence of any obvious contaminants contributed to ruling out the possibility that the molecular features in Figs 1, 4 and 5 were due to any contamination.

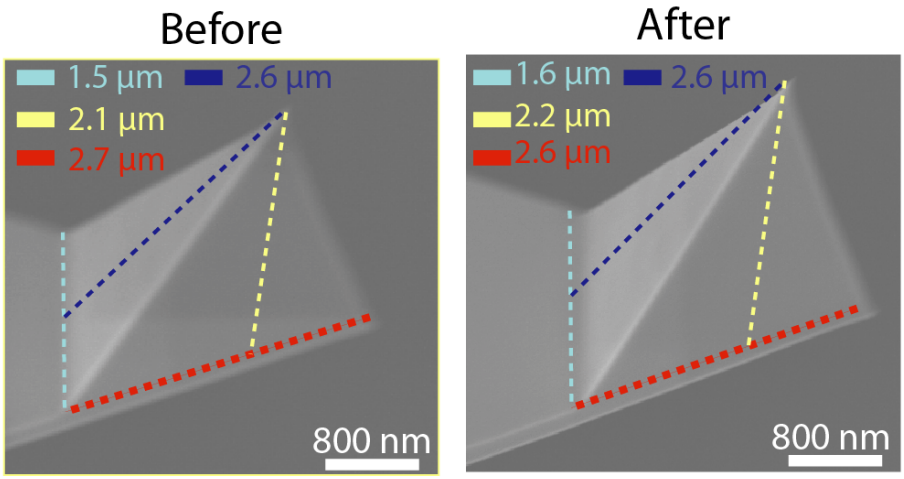

Fig. S6. Representative scanning electron microscopy images of the AFM probes. *The cantilevers were studied before and after conducting shear-force measurements with no clear changes visible. The contact area is quantified by fitting the base and apothem for the faces of the triangular probe with the dashed lines. The estimated value of the contact area is 100 ± 10 nm* [2] [8].

7. Thermodynamics calculations at the interface

7.1 Interfacial energies

Thermodynamics considerations about the most likely configurations of the different molecular species at the interface all hinge on the interfacial energies at play. Tables S1 gives the interfacial energy contributions γ for each of the key interfaces in the system.

Interface	γ (mN/m)
hexadecane-air[9]	27.42
hexadecane-mica*	53.90
hexadecane-water[10,11]	53.30
water-air[12]	71.97
water-mica[13,14]	83.00
mica-air[13]	173.00

Table S1. *Interfacial energies between the different materials present in the system at 25 °C.*
** experimentally determined in this study from contact angle measurements.*

7.2 Work of adhesion and wetting

The quantity that describes the affinity between two media or, in the case of a solid-liquid interface, the wetting properties of the liquid is the so-called work of adhesion W. The work of adhesion $W_{1,2}$ between the media 1 and 2 is related to the interfacial energy through the Dupré equation[7,15,16]:

$$\gamma_{1,2} = \gamma_1 + \gamma_2 - W_{1,2} \qquad (s3)$$

where γ_1 and γ_2 are respectively the surface energies of the media. The definition can be extended for interfaces exposed to a third medium (e.g. air) so that the work of adhesion between a solid and a liquid in the presence of a gas can be written as[7]:

$$W_{S_GL} = \gamma_{S,G} + \gamma_{L,G} - \gamma_{S_GL} \qquad (s4)$$

with $\gamma_{S,G} \sim \gamma_S$ the surface energy of the solid, $\gamma_{L,G}$ the surface tension (or surface energy) of the liquid measured in the presence of the gas and γ_{S_GL} the interfacial energy between the solid and the liquid in ambient conditions (not sealed from the atmosphere). From this last equation and the values given in table S1, we can estimate the following works of adhesion:

- Mica-water in air: $W_{m,a,w} = 162$ mN/m
- Mica-hexadecane in air: $W_{m,a,h} = 146$ mN/m

The values are estimates and carry an uncertainty of ~ 10 % (measured values).

7.3 Spreading coefficients

The spreading coefficient S of a given liquid on the surface characterises the tendency of the liquid to spread on the solid, with spreading spontaneously occurring if $S > 0$. In the presence of a gas, S is simply derived from the Young's equation[17] assuming a null contact angle:

$$S_{L_G S} = \gamma_{SG} - \gamma_{LG} - \gamma_{SL} \qquad (s5)$$

where γ_{SG}, γ_{LG}, γ_{SL} correspond to the different interfacial energies between the solid, the liquid and the gas (S, L and G respectively). For water and hexadecane over mica in air, and using the values of table S1, we get:

- $S_{w,a,m} = 18$ mN/m
- $S_{h,a,m} = 92$ mN/m

The values are estimates and carry an uncertainty of ~ 10 % (measured values).

7.4 Calculation of the total interfacial energy for a uniform water film vs a nanodroplet

At the beginning of each experiment, the mica surface is covered with a thin layer of water, typically 2 to 10 molecules thick (0.4 nm to 2 nm) depending on the ambient humidity[18,19]. After immersion of the system into hexadecane, the layer may condense into discrete nanodroplets. Here we calculate and compare the free energy associated with a same area A of the interface covered by either (i) a uniform water layer of thickness w or (ii) a single nanodroplet with the shape of a spherical cap as shown in Fig. S7. The total volume of water and hexadecane is conserved between the two situations, but the area of the different interfaces changes.

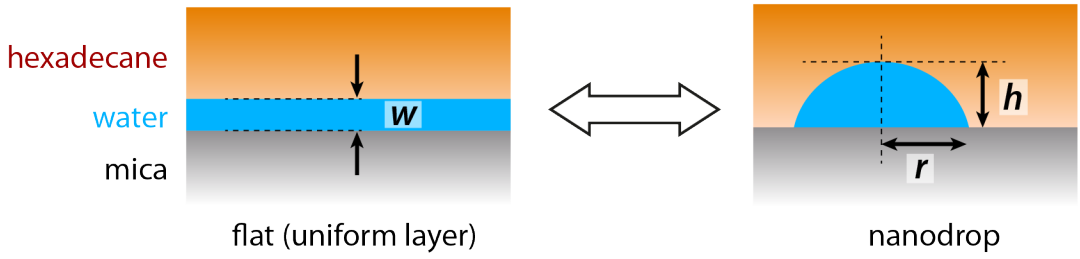

Fig. S7. Cartoon representation of the different interface configurations. *Water initially forms a thin uniform layer covering the whole mica surface (left) when the system is immersed in hexadecane. Another configuration is possible (right) with the water layer transitioning to discrete water nano-droplets.*

Using the notation given in Fig. S7, the free energy E_{flat} associated with the uniform (flat) interface is given by:

$$E_{flat} = A\gamma_{m,w} + A\gamma_{h,w} \qquad (s6)$$

where the indices m, w and h stand for mica, hexadecane and water, respectively. To calculate the free energy E_{drop} associated with the interface containing the water droplet, it is necessary to first calculate the area of the droplet in contact with the mica and with the hexadecane. Assuming a spherical cap shape, the area covered by the water-hexadecane interface is given by $\pi(r^2 + h^2)$, the area of water-mica contact is the base of the cap πr^2 and the hexadecane-mica area is simply given by $A - \pi r^2$. This leads to the following expression:

$$E_{drop} = \pi r^2\gamma_{m,w} + (A - \pi r^2)\,\gamma_{m,h} + \pi(r^2 + h^2)\,\gamma_{h,w} \qquad (s7)$$

Finally, both equations s6 and s7 can be made independent of the area A of the interfacial region considered by assuming a conservation of the water volume:

$$Aw = \frac{1}{6}\pi h(3r^2 + h^2) \qquad (s8)$$

where the left term of the equality is the volume of water contained in the flat layer and the right-hand side term the volume of the cap making the water nanodroplet.

Combining the equations s6-s8 and the interfacial energies given in Table S1, it is straightforward to calculate the ratio E_{flat}/E_{drop} as a function of r, h and w. The ratio was calculated for (Figs. 2 and S7):

- r ranging between 0.2 nm (1 water molecule) and 15 nm (30 nm diameter droplet, seen experimentally)
- h ranging between 0.2 nm (1 water molecule) and 5 nm (larger droplets observed experimentally)
- w = 2, 4, 6, 8 and 10 water layers so that 0.4 nm ≤ w ≤ 2 nm

In all cases, if $E_{flat}/E_{drop} < 1$, the uniform water film is thermodynamically favoured. These regions of the parameter space appear as blue in Fig. S8. If $E_{flat}/E_{drop} > 1$, water droplets are favoured with the associated regions of the parameter space appearing red in Fig. S8. The boundary between the two configurations is simply given by $E_{flat}/E_{drop} = 1$.

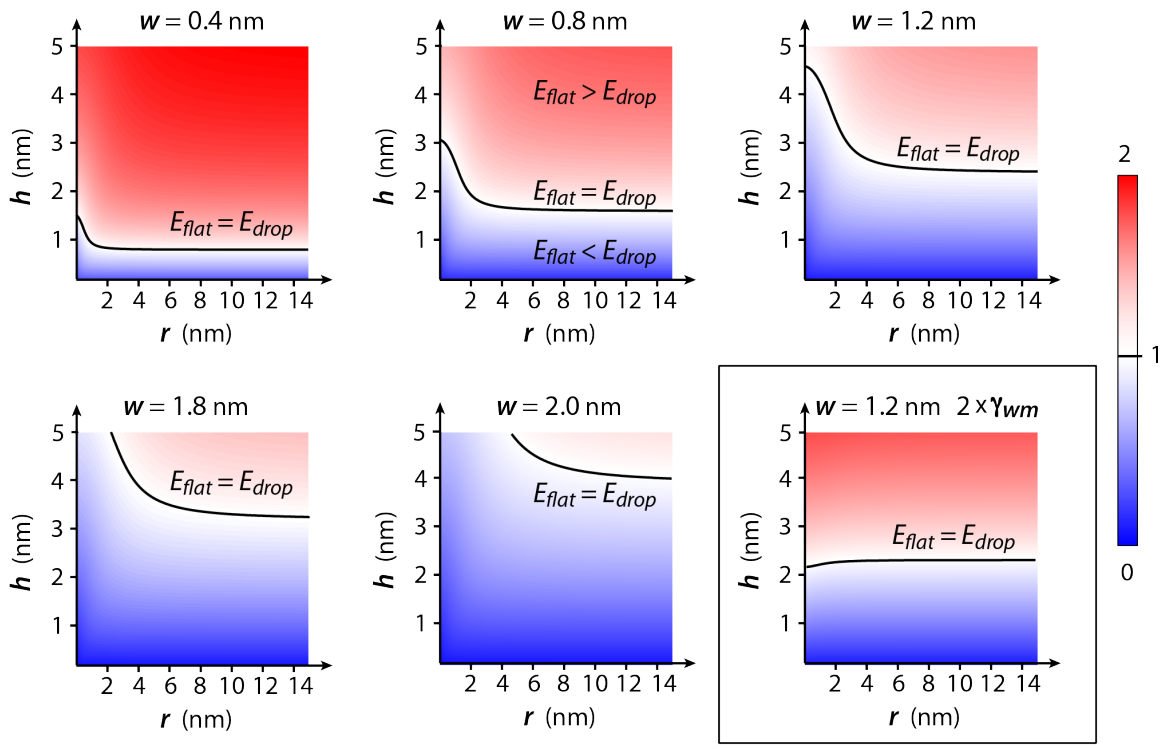

Fig. S8. Energy landscape of the interface. *The energy ratio* E_{flat}/E_{drop} *is plotted as a function of* r *and* h *for different* w *values reflecting typical experimental conditions. The regions appearing in blue favour a uniform water layer to cover the mica surface whereas red regions favour the formation of discrete water droplets. Higher humidity conditions (larger* w *values) favour larger droplets and flatten the energy landscape. Increasing by a factor of two the interfacial energy between water and the solid (hence lowering the water-solid affinity) tends to shift the equilibrium to smaller droplets and reduce the influence of* h*, rendering their nucleation more likely.*

8. van der Walls interactions as a function of the Hamaker constant

The potential associated with the van der Walls interactions between two media 1 and 2 separated by a distance L through a third medium 3 can be described as[20]

$$E_{1,3,2} = -\frac{H_{1_3 2}}{12\pi L^2} \qquad (s9)$$

where $H_{1,3,2}$ is the Hamaker constant[20,21]:

$$H_{1,3,2} \cong \frac{3k_BT}{4}\,\frac{\epsilon_1-\epsilon_3}{\epsilon_1+\epsilon_3}\,\frac{\epsilon_2-\epsilon_3}{\epsilon_2+\epsilon_3} + \frac{3h\,\nu_\epsilon}{8\sqrt{2}}\,\frac{(n_1^2-n_3^2)(n_2^2-n_3^2)}{\sqrt{n_1^2+n_3^2}\,\sqrt{n_2^2+n_3^2}\,(\sqrt{n_1^2+n_3^2}\,\sqrt{n_2^2+n_3^2})} \qquad (S10)$$

where k_B, T, h, ν_ε, ε_i and n_i are the Boltzmann constant, the temperature, the Planck constant, the electronic absorption frequency, the dielectric constant and the refractive index, respectively. The ε_i and n_i values for all the interfacial components are shown in Table S2.

medium	ε_i	n_i
Air	1.0 [21]	1.000 [21]
Hexadecane	2.1 [23]	1.423 [22,23]
Mica	7.0 [24,25]	1.598 [26,27]
Water	80.0 [22,23]	1.333 [22,23]

Table S2. *Dielectric constant and refractive index values for the different components of our model system.*

Air is taken to have dielectric constant of 1 [21]. The electronic absorption frequency for hexadecane and water was taken to be $3e^{15}$ Hz[23].

9. Hexadecane spreading at different humidity (videos 1-2-3)

The three attached video files show hexadecane spreading at relative humidity *RH* of 0%, 46% and 100%, respectively. All the experiments were performed at 25 °C. The mica disc was incubated for 30 minutes at the desired room humidity and temperature before depositing 5 µl of hexadecane on it.

Video 1 - hexadecane spreading at *RH* = 0%. Frame rate: 1 Hz ~ 1 image/second
Video 2 - hexadecane spreading at *RH* = 46% Frame rate: 0.077 Hz ~ 1 image/13 seconds
Video 3 - hexadecane spreading at *RH* = 100%. Frame rate: 1 Hz~ 1 image/second

10. Impact of oleic acid on the shear phase

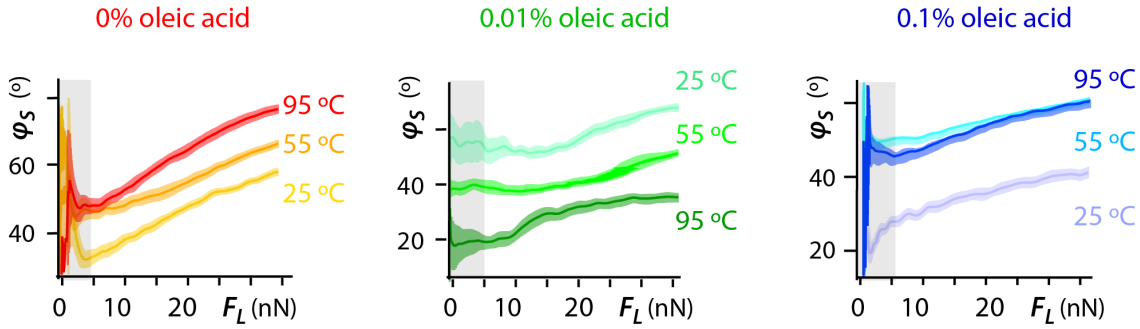

Fig. S9. Shear phase φ_S associated with the lubrication force presented in Fig. 5. *In the absence of any oleic acid, the shear phase values confirm a viscoelastic behaviour for all the different temperatures probed with a more pronounced viscous component as the temperature increases. Adding 0.01% oleic acid appears to reverse the trend, with higher temperatures appearing more elastic. This anomalous behaviour could be due to a partially compensated effect of the water nanodroplets which may create pinning points for the AFM tip[4]. At 0.1% oleic acid, the behaviour is back to a more usual trend with temperature, but without a regular progression.*
At low confining forces (< 5 nN), the shear amplitude and hence force are close to the experimental noise level. The shear phase is hence undefined (semi-transparent region). Experiments were performed at RH = 45± 2 %.

11. Mica coverage by oleic acid molecules

The mica substrate is a disc of 12 mm diameter, with a total area of ~113 mm^2. The oleic acid being at the interface between the water film on the surface of mica and the hexadecane, we assume the oleic acid molecules to be standing upright so as to minimise the interfacial energy. This hypothesis is further supported by previous adsorption studies of oleic acid on iron oxide where the molecules were found to adsorb in an upright position and with a molecular surface area of ~0.45 nm^2 per molecule at saturation[28]. Using this value, we find that the number of molecules N in an oleic acid layer covering the whole mica surface is given by $N \sim 113\times10^{12}$ nm^2 / 0.45 $nm^2 \sim 2.5\times10^{14}$. This value is an approximation but it provides a good indication of the order of magnitude for N.

For comparison, a 100 µl drop (volume of the experiment) of hexadecane with a 0.1% molar concentration of oleic acid would approximately contain $N \sim 2 \times 10^{16}$ oleic acid molecules in the solution[12]: $N \sim 10^{-4} \times 10^{-4}$ litre $\times$ 0.77 $\times 10^3$ g $litre^{-1}$ / 226 g $mol^{-1} \times 6 \times 10^{23} \sim 2 \times 10^{16}$.

This suggests that 1/100 oleic acid molecules are at the interface to create a cohesive layer. Given the entropic costs associated with having all the acid molecules at the interface, a ratio of 1/100 indicates a strong affinity of the acid for the interface if a full layer can form.

12. Supplementary references

1. T. D. Li and E. Riedo, *Phys. Rev. Lett.*, 2008, **100**, 106102.
2. T. D. Li, J. Gao, R. Szoszkiewicz, U. Landman and E. Riedo, *Phys. Rev. B*, 2007, **75**, 115415.
3. K. Voïtchovsky. *Nanoscale*, 2016, **8**, 17472-17482.
4. C. Cafolla, and K. Voïtchovsky. *Nanoscale*, 2018, **10**, 11831-11840.
5. C. Cafolla, W. Foster, and K. Voïtchovsky. *Sci. Adv.,* 2020, **6**, eaaz3673.
6. C. Cafolla, A. F. Payam, and K. Voïtchovsky. *J. Appl. Phys*., 2018, **124**, 154502.
7. J. N. Israelachvili. *Intermolecular and surface forces*. Academic Press, Cambridge Massachusetts, 3rd Edition, 2015.
8. A. C. Fischer-Cripps. *Introduction to contact mechanics*. Springer, Boston, 2000.
9. Surface Tension of Hexadecane from Dortmund Data Bank, http://www.ddbst.com/en/EED/PCP/SFT_C516.php, (Accessed: 8th May 2020).
10. G. M. Kontogeorgis, and S. Kiil. *Introduction to applied colloid and surface chemistry*. John Wiley & Sons, West Sussex, 2016.
11. R. Aveyard, and I. A. Haydon. *Trans. Faraday Soc.,* 1965, **61**, 2255-2261.
12. J. A. Dean. *Lange's handbook of chemistry*. McGraw-Hill, Inc., New York, 1999.
13. J. Drelich, G. W. Tormoen, and E. R. Beach. *J. Colloid Interface Sci.,* 2004, **280**, 484–497.
14. A. I. Bailey and S. M. Kay. *Proc. R. Soc. Lond.*, 1967, **301**, 47-56.
15. R. A. L. Jones, R. Jones, and R. A. L. Jones. *Soft condensed matter*. Oxford University Press, Oxford, 2002.
16. A. Dupré. *Théorie mécanique de la chaleur*. Gauthier-Villars, Paris, 1869.
17. T. Young. An Essay on the Cohesion of Fluids. *Phil. Trans. R. Soc. Lond.*, 1805, ***95***, 65–87.
18. T. Arai, K. Sato, A. Iida, and M. Tomitori. *Sci. Rep.,* 2017, **7**, 1-11.
19. X. Gong, A. Kozbial, and L. Li. *Chem. Sci.*, 2015, **6**, 3478–3482.

20. J. M. Fernández-Varea, and R. Garcia-Molina. *J. Colloid Interface Sci.,* 2000, **231**, 394–397.
21. L. Leite, C. C. Bueno, A. L. Da Róz, E. C. Ziemath, and O. N. Oliveira. *Int. J. Mol. Sci.,* 2012, **13**, 12773–12856.
22. C. J. Van Oss, M. K. Chaudhury, and R. J. Good. *Chem. Rev.,* 1988, **88**, 927-941
23. I. Lee. *J. Mater. Sci.,* 1995, **30**, 6019–6022.
24. C. G. Low, and Q. Zhang. *Small,* 2012, **8**, 2178–2183.
25. C. G. Low, Q. Zhang, Y. Hao, and R. S. Ruoff. *Small*, 2014, **10**, 4213–4218.
26. A. I. Bailey, and S. M. Kay. *J. Appl. Phys.,* 1965*,* **16**, 39.
27. S. L. Guo, B. L. Chen, and S.A. Durrani. In *Handbook of Radioactivity Analysis* Academic Press, Cambridge Massachusetts, 4th Edition, 2020, 3, 307-407.
28. M. H. Wood, M. T. Casford, R. Steitz, A. Zarbakhsh, R. J. L. Welbourn, and S. M. Clarke. *Langmuir*, 2016, **32**, 534-540.